

Convolutional Neural Network-reconstructed velocity for kinetic SZ detection

Hideki Tanimura¹, Nabila Aghanim¹, Victor Bonjean^{2,3}, and Saleem Zaroubi^{4,5}

¹ Université Paris-Saclay, CNRS, Institut d'Astrophysique Spatiale, Bâtiment 121, 91405 Orsay, France

² Instituto de Astrofísica de Canarias, E-38205 Tenerife, Spain

³ University of La Laguna, E-38206 Tenerife, Spain

⁴ ARCO (Astrophysics Research Center), Department of Natural Sciences, The Open University of Israel, 1 University Road, PO Box 808, Ra'anana 4353701, Israel

⁵ Kapteyn Astronomical Institute, University of Groningen, PO Box 800, NL-9700 AV Groningen, the Netherlands
e-mail: hideki.tanimura@ias.u-psud.fr

ABSTRACT

By stacking the latest 217 GHz *Planck* PR4 map at the positions of 30,431 galaxy clusters from the Wen-Han-Liu (WHL) catalog, we report the detection of the kinetic Sunyaev-Zel'dovich (kSZ) effect in galaxy clusters with a 4.9σ significance level and beyond $3 \times R_{500}$. The line of sight velocities of galaxy clusters were estimated with a machine-learning approach, in which the relation between the galaxy distribution around a cluster and its line-of-sight velocity was trained through a convolutional neural network using the simulated galaxies and galaxy clusters in the Magneticum cosmological hydrodynamic simulations. The trained model was applied to the large-scale distribution of the Sloan Digital Sky Survey galaxies to derive the line-of-sight velocities of the WHL galaxy clusters. Assuming a standard β -model for the intracluster medium, we found that the gas fraction within R_{500} is $f_{\text{gas},500} = 0.09 \pm 0.02$ for the clusters with the mass of $M_{500} \sim 1.0 \times 10^{14} h^{-1} M_{\odot}$.

Key words. galaxies: clusters: general - intracluster medium - Cosmology:large-scale structure of Universe - cosmic background radiation

1. Introduction

Galaxy clusters are the largest gravitationally bound structures in the Universe and have been used as probes of cosmology and astrophysics. These massive objects imprint their signature on the cosmic microwave background (CMB) through the Sunyaev-Zel'dovich (SZ) effect (Sunyaev & Zeldovich 1970, 1972, 1980). The SZ effect is caused by the scattering of CMB photons by hot and ionized plasma in the intracluster medium (ICM), giving rise to a change in the CMB temperature. The SZ effect is classified into two contributions: the thermal Sunyaev-Zel'dovich (tSZ) effect and the kinetic Sunyaev-Zel'dovich (kSZ) effect (Sunyaev & Zeldovich 1980).

The kSZ effect is caused by the scattering of CMB photons off the electrons due to the peculiar motion of a galaxy cluster, leading to a Doppler shift of the CMB blackbody spectrum. While the kSZ effect is elusive due to its small amplitude and identical spectral signature as the CMB, it has great potential in constraining both cosmological (Bhattacharya & Kosowsky 2008; Alonso et al. 2016; Ma & Zhao 2014; Mueller et al. 2015; Bianchini & Silvestri 2016; Madhavacheril et al. 2019; Kuruvilla & Aghanim 2021; Kuruvilla 2021) and astrophysical models. While the use of kSZ to constrain cosmological models is still limited due to the weakness of the signal, there are several studies using the kSZ effect to measure the optical depth or gas mass fraction in galaxy clusters (e.g., Planck Collaboration 2016c; Schaan et al. 2016; Soergel et al. 2016; De Bernardis et al. 2017; Sugiyama et al. 2018; Lim et al. 2020; Tanimura et al. 2021). Because the kSZ effect is sensitive to the virialized gas and also to the gas surrounding halos, independent of its temperature (un-

like the tSZ effect), it is well suited for studying the gas distribution around galaxy clusters. kSZ can hence potentially be used to solve a debate on whether a significant fraction of diffuse gas is present around halos as a circumgalactic medium or whether the gas, once expelled because of feedback processes such as star formation, supernovae, and active galactic nuclei (AGNs), is never accreted onto the halos (e.g., Planck Collaboration 2013; Anderson et al. 2015; Le Brun et al. 2015).

The kSZ signal has so far been detected for a few individual systems (e.g., Sayers et al. 2013; Adam et al. 2017) or by statistical measurements such as the pairwise method (e.g., Hand et al. 2012; Hernández-Monteagudo et al. 2015; Planck Collaboration 2016c; Soergel et al. 2016; De Bernardis et al. 2017) or cross-correlation method (Hill et al. 2016). In addition to these approaches, an optimized stacking analysis was used in Schaan et al. (2016), Schaan et al. (2021), and Tanimura et al. (2021) (hereafter T21). In T21, the authors estimated peculiar velocities of galaxy groups and clusters through the distribution of their surrounding galaxies from the Sloan Digital Sky Survey (SDSS) (Reid et al. 2016) based on the linearized continuity equation and used the peculiar velocities to align the signs of the kSZ signals and stack them. While a linearized continuity equation was used to estimate the peculiar velocities in those studies, a deep learning technique was recently used in Wu et al. (2021) to reconstruct the cosmic velocity field from the dark matter density field in numerical simulations.

In the present study, we extend this approach to real data using the training on galaxy distribution derived from hydrodynamical simulations instead of dark matter distribution. We use a new machine-learning approach to estimate the line-of-sight

(LOS) velocities of galaxy clusters based on their surrounding galaxy distribution. The purpose is to apply our trained model to actual data and use the estimated LOS velocities to detect the kSZ signal of galaxy clusters. The paper is organized as follows. Section 2 summarizes datasets used in our analyses. Section 3 explains the LOS velocity reconstruction of galaxy clusters. Section 4 and 5 present the stacking method and the detection of the kSZ signals. The interpretation of the measurements is presented in Section 6. We end this paper with discussions and conclusions in Section 7.

Throughout this work, all masses are quoted in units of solar mass divided by the present value of the Hubble parameter h , and M_Δ is mass enclosed within a sphere of radius R_Δ such that the enclosed density is Δ times the *critical* density at redshift z . For the Hubble constant, we used $H_0 = 70.4 \text{ km s}^{-1} \text{ Mpc}^{-1}$ from Komatsu et al. (2011) in our data analysis, but we obtain consistent results using the value from the *Planck* cosmology in Planck Collaboration (2016a). Uncertainties are given at the 1σ confidence level.

2. Data

2.1. Galaxy cluster catalog

A total of 158,103 galaxy groups and clusters (hereafter WHL galaxy clusters) was identified in Wen et al. (2012) and Wen & Han (2015) using the SDSS galaxies in the redshift range between 0.05 and 0.8, of which 89% have spectroscopic redshifts. The masses of the WHL galaxy clusters were estimated from their total luminosity and were calibrated by the masses of 1191 clusters using X-ray or tSZ measurements. From this cluster catalog, T21 selected the WHL galaxy clusters with spectroscopic redshifts at $0.25 < z < 0.55$ and masses of $M_{500} > 10^{13.5} h^{-1} \text{ M}_\odot$. They also removed galaxy clusters if their surroundings were largely masked by the Galactic and point source masks produced by the *Planck* collaboration for their analysis of the CMB and SZ maps (see Sect. 2.3 for the masks). This selection resulted in the 30,431 galaxy clusters used in T21, which we also use in the present study.

2.2. Galaxy catalog

To estimate the peculiar velocities of WHL galaxy clusters, T21 used the Baryon Oscillation Spectroscopic Survey (BOSS) LOWZ galaxies and constant-mass (CMASS) galaxies in Reid et al. (2016), composed of 953,193 galaxies in the northern Galactic hemisphere and 372,542 in the southern Galactic hemisphere. The completeness of the galaxies is stated to be 99% for CMASS and 97% for LOWZ. Spectroscopic data are available for all the galaxies, and their redshifts extend up to $z \sim 0.8$. T21 limited their analysis to the redshift range of $0.25 < z < 0.55$, in which the number density of the galaxies in the survey volume is fairly flat (see Fig. 11 in Reid et al. 2016). In the present analysis, we also limit to this redshift range.

2.3. Planck maps from PR3

T21 used the *Planck* all-sky map at 217 GHz from the Planck 2018 data release (Planck Collaboration 2018) for the detection of the kSZ signal¹. This frequency corresponds to the null frequency of the tSZ effect. To minimize the Galactic and extra-

galactic contamination, T21 applied the mask produced by the *Planck* team for the analysis of the CMB temperature maps, which masks the region around the Galactic plane and the point sources detected at all the *Planck* frequencies (see Table C.1 in Planck Collaboration 2020a). In addition, T21 used a more robust point-source mask, masking radio and infrared sources used for the analysis of the Compton y maps (Planck Collaboration 2016b). Combining these two masks excludes $\sim 50\%$ of the sky. We also use these *Planck* maps and masks to compare our results with those of T21.

2.4. Planck maps from PR4

We also apply our new approach on the latest *Planck* PR4 data (Planck Collaboration 2020b)³. The *Planck* PR4 data include several improvements compared to the previous data release: the usage of foreground polarization priors during the calibration stage to break scanning-induced degeneracies, the correction of bandpass mismatch at all frequencies, and the inclusion of 8% more data collected during repointing maneuvers, etc. These improvements reduced noise and systematic effects in the frequency maps at all angular scales and yielded better internal consistency between the various frequency bands.

Planck collaboration split data into two and produced two maps at each frequency, called half-ring maps. The difference between the two half-ring maps cancels out the astrophysical emissions and can be used as noise maps of the band maps. We use these noise maps for our null tests.

2.5. Magneticum simulation

For the training and test of our machine-learning approach, we use the Magneticum simulations. The simulation is one of the largest cosmological hydrodynamical simulations (Hirschmann et al. 2014; Dolag 2015), and is based on the standard Λ CDM cosmology from Komatsu et al. (2011) with $\Omega_m = 0.272$, $\Omega_b = 0.046$, and $H_0 = 70.4 \text{ km s}^{-1} \text{ Mpc}^{-1}$. Several simulation boxes with different sizes and resolutions⁴ were produced, of which we use “Box0” with the largest box-size of $2,688 h^{-1} \text{ Mpc}$ using $2 \times 4,536^3$ particles for dark matter and baryons, including the post-processed data of the galaxy catalog and the cluster catalog. In particular, we used the simulation data from “snapshot 25” at $z \sim 0.47$, corresponding to the median redshift of the WHL galaxy clusters used in our analysis.

3. Machine-learning reconstructed LOS velocities

3.1. Training with the Magneticum simulation

We trained our network to learn the correlation between the LOS velocities of galaxy clusters and their surrounding galaxies using the Magneticum simulation. The 3-dimensional velocity of galaxy clusters (v_x , v_y , and v_z) is provided by the simulation. We define v_z as LOS velocity in the simulation. Note that we did not train for velocities in other directions than LOS because they are irrelevant for our purpose to detect the kSZ signal.

First, we reproduced the selection performed on the “real” data to construct “mock” data. We removed simulated galaxy clusters with $M_{500} < 10^{13.5} h^{-1} \text{ M}_\odot$ (minimum mass of the WHL

¹ This map was provided in HEALpix² format (Górski et al. 2005) with a pixel resolution of $N_{\text{side}} = 2048$ (~ 1.7 arcmin).

³ https://irsa.ipac.caltech.edu/data/Planck/release_3/ancillary-data/HFI_Products.html#hfi_allsky_maps

⁴ The associated data are available at <http://www.magneticum.org/simulations.html>

galaxy clusters in our analysis) and also removed simulated galaxies with $M_* < 1.0 \times 10^{10} h^{-1} M_\odot$ so that the number density of galaxies is the same as the real data.

Second, we constructed a grid coordinate system around each galaxy cluster from the simulations as in T21. The authors placed a galaxy cluster at the center in a cubic box of $\sim 250^3 h^{-1} \text{Mpc}$, in which the 3-dimensional box was divided into grid cells of $5^3 h^{-1} \text{Mpc}$. Then, T21 placed galaxies around the galaxy cluster in the box cells and calculated the galaxy overdensities. The grid size was determined to be large enough compared to the length expected from redshift-space distortion (RSD): The RSD for a typical velocity of 300 km/s is $\sim 3 h^{-1} \text{Mpc}$ at the corresponding redshift range. Box cells were then smoothed by a Gaussian kernel of $2 h^{-1} \text{Mpc}$ to remove sharp grid edges. In our present analysis, the grid size is modified to be $10 h^{-1} \text{Mpc}$ because the same grid size as T21 causes a memory issue during our training process.

Third, we split the simulation box of $2,688 (h^{-1} \text{Mpc})^3$ into eight independent regions and used seven for the training and validation (the number of galaxy clusters in this volume is 418,374) and one for the test (where the number of galaxy clusters is 59,767).

Finally, we input a series of 25^3 voxels corresponding to the 3-dimensional galaxy overdensity fields around galaxy clusters into our convolutional neural network and train our network for the LOS velocities of the galaxy clusters. For comparison, we changed the size of the box from $250^3 h^{-1} \text{Mpc}$ to $210^3 h^{-1} \text{Mpc}$ and $\sim 290^3 h^{-1} \text{Mpc}$, but our kSZ measurements were consistent within the 1σ uncertainty.

3.2. Neural network architecture

We adopt a convolutional neural network (CNN) architecture (Chollet 2018). The overall structure of our network is designed as follows.

A series of 25^3 voxels, corresponding to galaxy overdensity fields with a size of $250^3 h^{-1} \text{Mpc}$, are fed into a CNN with three convolutional layers to capture the abundant features in the 3-dimensional fields. Each convolutional layer is designed to have a “relu” activation function and “same” padding so that the outputs have the same dimension as the inputs. Then, each layer is passed to the Maxpooling layer to decrease the dimension by half. This step helps reduce the number of parameters to learn and the amount of computations performed in the network. The first, second, and third layer consists of 16, 32, and 64 filters, respectively, each of which has a shape of 3^3 . We changed the number of filters from 16, 32, 64 to 32, 64, 128, but our kSZ measurements were consistent within the 1σ uncertainty. Thus, we used the lower number of filters to reduce the number of parameters to learn and the amount of computations in the network. Finally, the output of the three convolutional layers is fed into two fully-connected dense neural layers: the first layer with 64 output units and the second with one output unit, which corresponds to the LOS velocity of a galaxy cluster. The learning process is configured with the optimizer and loss function that our model uses. We use “rmsprop” for optimizer and “mse” for loss function.

3.3. Test with the Magneticum simulation

We checked the validity of our machine-learning approach using the test-set in the Magneticum simulation.

The first test was performed with the mock galaxies in the simulations. We applied our trained model in Sect.3.1 to the galaxy clusters and their surrounding galaxy overdensity fields in the test-set and estimated their LOS velocities. The result is displayed in the left panel of Fig. 1. The figure shows a positive correlation between the true (v_{true}) and estimated (v_{CNN}) LOS velocities. To check the bias in the estimated velocities, we fit them with a linear equation and found little bias with $v_{\text{CNN}} = 1.01 \times v_{\text{true}} + 5.7 \text{ [km/s]}$. The difference between the true and estimated velocities gives the uncertainty associated with our approach, which was estimated to be $\Delta v \sim 189 \text{ km/s}$. For comparison, we used the method in Section 3 of T21 and estimated the LOS velocities of the galaxy clusters (v_{T21}) in the same test-set. The result is shown in the left panel of Fig. 2. Again, to check the bias in the estimated velocities, we fit the true and estimated velocities with a linear equation, and almost no bias was found with $v_{\text{T21}} = 0.99 \times v_{\text{true}} - 27.0 \text{ [km/s]}$. The uncertainty in the estimated velocities was obtained to be $\Delta v \sim 187 \text{ km/s}$, nearly equivalent to the value derived with our machine-learning approach.

Then, to construct the model to apply for the actual data, we added RSD to the galaxies (Eq. 11 in Hogg 1999) in the simulations and re-trained our model. Note that we did not re-identify galaxy clusters in the redshift space but used the same galaxy clusters with their positions redshifted. We applied our re-trained model to the galaxy clusters and their galaxy overdensity fields in the test-set and estimated their LOS velocities. The result is displayed in the right panel of Fig. 1. The estimated LOS velocities show a positive correlation with the true LOS velocities, but give a slightly lower value with $v_{\text{CNN}} = 0.95 \times v_{\text{true}} + 19.0 \text{ [km/s]}$. The uncertainty in the estimated velocities was obtained to be $\Delta v \sim 232 \text{ km/s}$. For comparison, we again used the method in T21 and estimated the LOS velocities of the galaxy clusters in the same test-set. The result is shown in the right panel of Fig. 2. The estimated LOS velocities show a slightly higher value than the true LOS velocities with $v_{\text{T21}} = 1.14 \times v_{\text{true}} - 40.1 \text{ [km/s]}$. The uncertainty in the estimated velocities was obtained to be $\Delta v \sim 302 \text{ km/s}$. In summary, the bias in the estimated LOS velocities with our machine-learning approach is reduced to $\sim 5\%$ compared to the one of $\sim 14\%$ with the method in T21. In addition, its uncertainty with our machine-learning approach is reduced to $\Delta v \sim 232 \text{ km/s}$ compared to the one of $\Delta v \sim 302 \text{ km/s}$ with the method in T21, indicating an improvement with our machine-learning approach compared to the method in T21.

3.4. LOS velocities of WHL galaxy clusters

We applied our trained model in Sect.3.1 to the SDSS galaxy distribution around the WHL galaxy clusters to estimate the cluster’s LOS velocities from machine learning. The cluster’s LOS velocities can also be computed as in T21. These estimated velocities are compared in Fig. 3, and their relation is shown to be $v_{\text{CNN}} = 0.86 \times v_{\text{T21}} + 41.7 \text{ [km/s]}$. The LOS velocities from machine learning are slightly lower by 14% than those estimated with T21’s approach. This result is expected from the tests in Sect.3.3 using the test-set in the Magneticum simulations. Because our machine-learning approach estimated the LOS velocities lower by $\sim 5\%$ than the true values, and the T21’s approach did higher by $\sim 14\%$, the expected difference between these approaches is a factor of $0.95/1.14 \sim 0.83$, similar to the value of ~ 0.86 in Fig. 3.

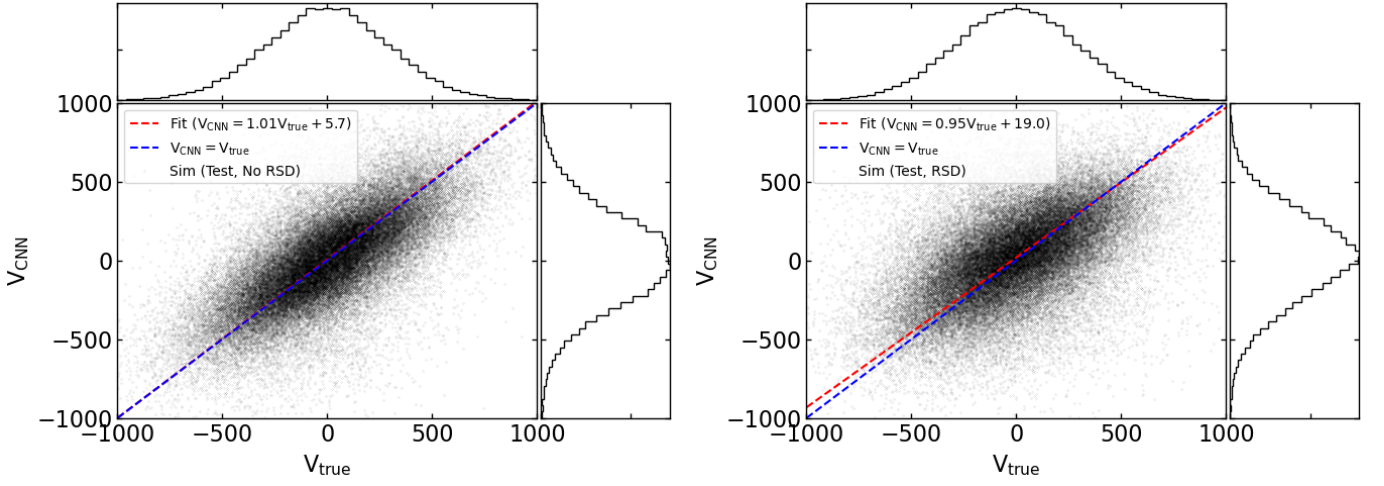


Fig. 1. X-axis: True LOS velocities of simulated galaxy clusters in the Magneticum simulations. Y-axis: Estimated LOS velocities of the same galaxy clusters with our machine-learning approach in Sect.3.1 when the RSD effect is not included (*left*) and included (*right*). The projected distributions along the X-axis and Y-axis are shown on the top and right panels. In addition, the result of the linear fit is shown between the true and estimated LOS velocities in the red-dashed line, which is compared to the case when they are equal shown in the blue-dashed line.

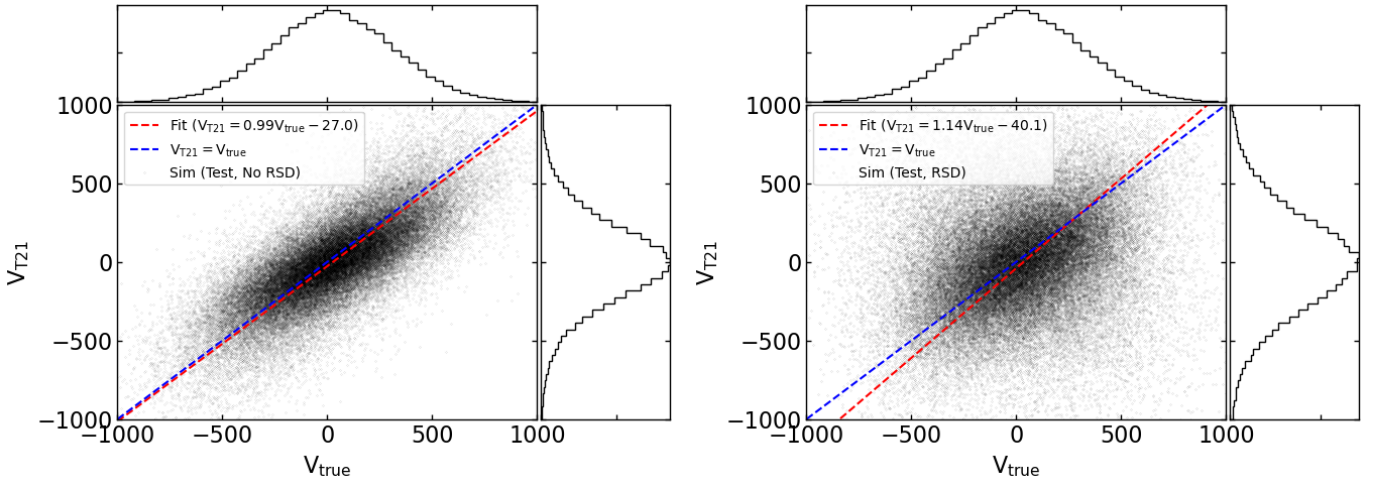


Fig. 2. X-axis: True LOS velocities of simulated galaxy clusters in the Magneticum simulations. Y-axis: Estimated LOS velocities of the same galaxy clusters computed using the method in T21 with the galaxy bias of $b = 2$ when the RSD effect is not included (*left*) and included (*right*). The projected distributions along the X-axis and Y-axis are shown on the top and right panels. In addition, the result of the linear fit is shown between the true and estimated LOS velocities in the red-dashed line, which is compared to the case when they are equal shown in the blue-dashed line.

4. Stacking analysis

We performed the stacking analysis to detect the kSZ signals from the WHL galaxy clusters using the same method as in T21 but replacing their LOS velocities with those estimated from our machine-learning approach. We stacked the *Planck* map from PR3 used in T21 and also the *Planck* map from the latest PR4. The latest *Planck* data have reduced statistical and systematic uncertainties, which provide more accurate and precise kSZ measurements.

Following T21, we first applied the filter shown in Fig. 2 of T21 to the *Planck* PR3 and PR4 maps. This filter reduces the contaminating contribution from the primordial CMB fluctuations. The amplitude of the primordial CMB fluctuations is of the order of ~ 100 μ K, while the amplitude of the kSZ signal around galaxy clusters is of the order of ~ 1 μ K, much weaker than the CMB. Thus, to increase the signal-to-noise of the kSZ signal, we filtered out signals at large scales above 30 arcmin

($\ell \sim 360$), dominated by the CMB, and kept signals at small angular scales below 15 arcmin ($\ell \sim 720$), where the kSZ signal from the WHL galaxy clusters is dominant. (The angular size of the virial radius of the WHL galaxy clusters is $2.2 - 10.5$ arcmin.) With this filter, the standard deviation of the primordial CMB fluctuations is reduced to ~ 40 μ K.

Second, we placed each galaxy cluster at the center of a two-dimensional grid in “scaled” angular distance in the range of $-10 < \theta/\theta_{500} < 10$, divided into 10×10 bins, where θ_{500} is the angular radius of a galaxy cluster calculated with R_{500} provided in the WHL cluster catalog. The *Planck* maps were scaled accordingly, and the data were placed on the two-dimensional grids, while the data in the masked region were not used.

Third, the stacking of the grid maps is performed for each cluster but weighted by the LOS velocity as follows.

$$T(R) = \frac{\sum_i T_i(R) \times v_{i, \text{LOS}} / \sigma_i^2}{\sum_i |v_{i, \text{LOS}}| / \sigma_i^2}, \quad (1)$$

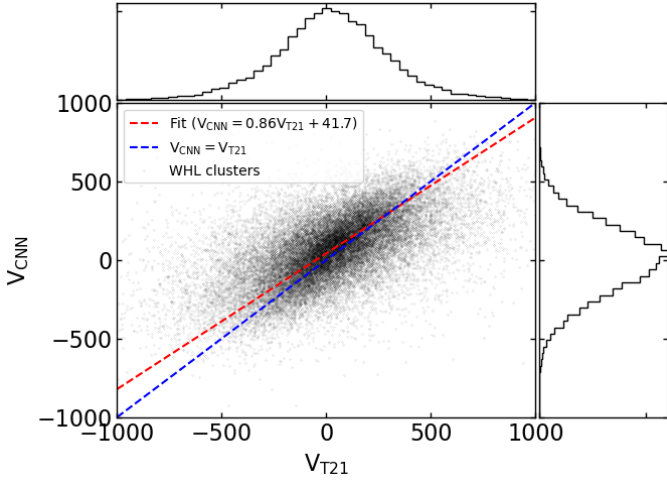


Fig. 3. Estimated LOS velocities of the WHL galaxy clusters with our machine-learning approach and the method in T21. The projected distributions along the X-axis and Y-axis are shown on the top and right panels. In addition, the result of the linear fit is shown between the two approaches in the red-dashed line, which is compared to the case when they are equal shown in the blue-dashed line.

where $T_i(R)$ is the temperature value of the i -th cluster at the radial distance, R , $v_{i, \text{LOS}}$ is the LOS velocity of the i -th cluster, and σ_i is the variance of temperature values within the region we consider ($10 \times \theta_{500}$) centered on the i -th cluster. The weight allows to align the signs of the kSZ signals given that there is an equal probability that a cluster will have a positive or negative LOS velocity, and the associated kSZ signal from clusters cancels out by a simple stacking⁵. A positive kSZ signal weighted by a negative LOS velocity has a negative signal, and a negative kSZ signal weighted by a positive LOS velocity also has a negative signal. Therefore, the kSZ signals can be stacked without any cancelation, while other components are canceled out. As an additional advantage, a galaxy cluster with a low LOS velocity (i.e., a weak kSZ signal) is underweighted in this stacking.

Finally, the stacked radial profile of the WHL galaxy clusters is computed. We assessed the uncertainties of the stacked profile through bootstrap resampling: We drew a random sample of the galaxy clusters with replacement and re-calculated one stacked profile for the new set of galaxy clusters. We repeated this process 1,000 times and produced the bootstrapped 1,000 stacked profiles, with which the covariance between different radial bins was computed.

5. kSZ detection from WHL galaxy clusters

5.1. kSZ detection with Planck PR3 maps

We stacked the *Planck* PR3 data at 217 GHz using the LOS velocities from T21 (T21 PR3) and our machine-learning approach (CNN PR3) in Fig. 4. As expected, the reduced uncertainties in the CNN-derived velocity estimate induce a better signal-to-noise in the kSZ measurements. The oscillating angular pattern seen in the stacked radial profile is the result of the convolution

⁵ We define “positive” LOS direction as a radial direction from us: a positive motion is a motion moving away from us, and a negative motion is a motion approaching us. It follows that when a galaxy cluster has a positive motion, the CMB is redshifted, resulting in a negative kSZ signal. On the other hand, when a galaxy cluster has a negative motion, the CMB is blueshifted, resulting in a positive kSZ signal.

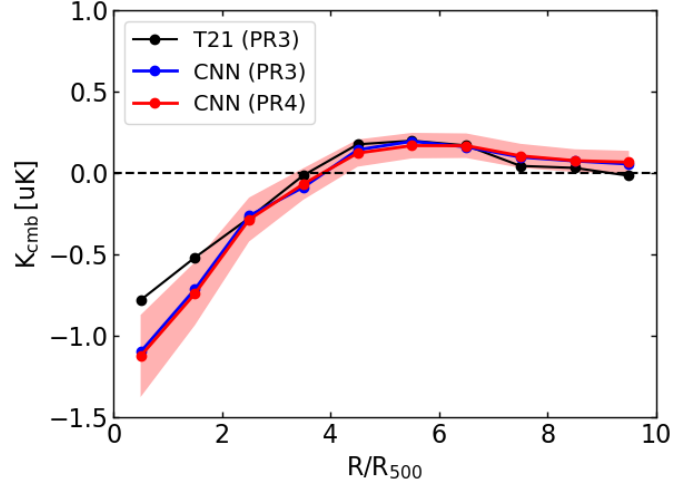


Fig. 4. Velocity-weighted kSZ radial profile around the 30,431 WHL galaxy clusters using the CNN-estimated LOS velocities and the *Planck* PR4 temperature map at 217 GHz (CNN PR4, red). The 1σ uncertainty is estimated by a bootstrap resampling. It is compared to the kSZ radial profile using the CNN-estimated LOS velocities and the *Planck* PR3 temperature map at 217 GHz (CNN PR3, blue). It is also compared to the kSZ radial profile in T21 using the *Planck* PR3 temperature map at 217 GHz (T21 PR3, black).

of kSZ and CMB with the filter, as discussed in T21. We refer to this profile as “velocity-weighted kSZ profile”, from now on.

We estimated the excess of the measured velocity-weighted kSZ profile with respect to the null hypothesis. The signal-to-noise ratio can be estimated as

$$S/N = \sqrt{\chi_{\text{data}}^2 - \chi_{\text{null}}^2}, \quad (2)$$

where

$$\chi_{\text{data}}^2 = \sum_{i,j} T_{\text{data}}(R_i)^T (C_{ij}^{-1}) T_{\text{data}}(R_j), \quad (3)$$

$$\chi_{\text{null}}^2 = \sum_{i,j} T_{\text{null}}(R_i)^T (C_{ij}^{-1}) T_{\text{null}}(R_j), \quad (4)$$

where $T_{\text{data}}(R_i)$ is the temperature value at the R_i bin of the data kSZ profile, $T_{\text{null}}(R_i)$ is the temperature value at the R_i bin under the null hypothesis, which is zero, and C_{ij} is the covariance matrix of the data profile, estimated by the bootstrap resampling. By measuring the kSZ signal up to $4 \times \theta_{500}$, the signal-to-noise ratio was estimated to be $\sim 4.7\sigma$, compared to $\sim 3.5\sigma$ in T21.

5.2. kSZ detection with Planck PR4 maps

We replaced the *Planck* map from PR3 with the one from the latest PR4 and performed the stacking analysis. The result is shown in Fig. 5. The 1σ statistical uncertainty is shown as the shaded area, corresponding to the square root of diagonal terms of the covariance matrix estimated by a bootstrap method.

To confirm the excess, we performed three Monte Carlo-based null tests, as in T21. In the first null test, we displaced the centers of the galaxy clusters at random positions on the sky and then stacked the *Planck* maps at these random positions. This process is repeated 1000 times to assess the *rms* fluctuations of the foreground and background signals. This result is shown in cyan in the left panel of Fig. 5 with the *rms* fluctuations. In the second null test, we randomly shuffled the LOS velocities of the

galaxy clusters, and then the clusters were stacked with weights based on the shuffled LOS velocities. This process sets the correlation between LOS velocities and clusters to zero. This shuffling process was repeated 1,000 times, and we evaluated the mean and standard deviation of the 1,000 stacked profiles with shuffled velocities. The result is shown in *yellow* in the middle panel of Fig. 5 with the rms fluctuations. In the third null test, we stacked a noise map produced from $(T_{217}^{\text{HM1}} - T_{217}^{\text{HM2}})/2$, where $T_{217}^{\text{HM1(2)}}$ is the half mission 1(2) *Planck* map at 217 GHz. The result is shown in the right (*green*) panels of Fig. 5 with the one σ uncertainties. As a conclusion from the three null tests, the average of the null-test profiles is consistent with zero, suggesting that our measurements are unbiased.

Finally, we estimated the excess of the measured velocity-weighted kSZ profile to the null hypothesis. The signal-to-noise ratio was estimated to be $\sim 4.9\sigma$.

6. Gas mass fraction in WHL galaxy clusters

In this section, we model our kSZ measurements and estimate the gas mass fraction in the WHL galaxy clusters.

The relative variation of CMB temperature due to the kSZ effect is given by

$$\frac{\Delta T_{\text{kSZ}}}{T_{\text{CMB}}} = -\sigma_T \int n_e \left(\frac{\mathbf{v} \cdot \hat{\mathbf{n}}}{c} \right) dl \simeq -\tau \left(\frac{\mathbf{v} \cdot \hat{\mathbf{n}}}{c} \right), \quad (5)$$

where σ_T is the Thomson scattering cross section, c is the speed of light, n_e is the electron number density, and $\mathbf{v} \cdot \hat{\mathbf{n}}$ represents the peculiar velocity of electrons along the line of sight. The integral, $\tau = \sigma_T \int n_e dl$, is performed assuming that the typical correlation length of LOS velocities (given by $\mathbf{v} \cdot \hat{\mathbf{n}}$) is much larger than the gas density correlation length ($\sim 5h^{-1}\text{Mpc}$). Thus, the velocities can be considered to be almost constant. This assumption is justified by Planck Collaboration (2016c) who showed that the typical correlation length of peculiar velocities is 80–100 $h^{-1}\text{Mpc}$, well above the gas correlation length.

The density profile in galaxy clusters can be expressed with a β model (Cavaliere & Fusco-Femiano 1978) given by

$$n_e(r) = n_{e,0} \left[1 + \left(\frac{r}{r_c} \right)^2 \right]^{-3\beta/2}, \quad (6)$$

where $n_{e,0}$ is the central electron density, r is the cluster radial extension, and r_c is the core radius of the electron distribution. We used $\beta = 0.86$ and $r_c = 0.2 \times R_{500}$ from the measurements of the South Pole Telescope clusters (Plagge et al. 2010). The observed profile is given by the geometrical projection of the 3-dimensional density profile, which is given by

$$\tau(R) = \sigma_T \int \frac{2r n_e(r)}{\sqrt{r^2 - R^2}} dr, \quad (7)$$

where R is the tangential distance from a galaxy cluster. (We represent the 3D distance with the lowercase letter r , and the 2D distance on a map with the uppercase letter R .)

We fit the β model to the measured kSZ profile. For the LOS velocity term in Eq. 5, we used the average LOS velocity (in absolute value) of the WHL galaxy clusters from Sect.3.4. However, the uncertainties on the LOS velocities induce a decrease in the amplitude of the measured kSZ signal (Nguyen et al. 2020) due to the stacks of kSZ signals with wrong signs. This effect can be analytically corrected using the uncertainty value of the LOS velocities estimated from the Magneticum simulation in Sect.

3.3. Including this correction in the model, the result of the fit is shown in Fig. 6. The reduced χ^2 value is 0.5. Note that a coherent angular pattern in the model profile, similar to the data profile, is due to the convolution of the β profile with our filter. The optical depth of a intracluster gas in the cluster within R_{500} is defined as

$$\tau_{e,500} = \int_0^{R_{500}} \sigma_T n_e(r) dV, \quad (8)$$

and the fit provides an average optical depth of the WHL galaxy clusters of

$$\bar{\tau}_{e,500} = (2.0 \pm 0.4) \times 10^{-3}. \quad (9)$$

The total gas mass in a galaxy cluster can be defined as

$$M_{\text{gas},500} = \int_0^{R_{500}} n_e(r) \mu_e m_p dV, \quad (10)$$

where $\mu_e = 1.148$ is the mean molecular weight of electrons (Arnaud et al. 2010), and m_p is the mass of proton. From this equation, we can thus compute the average gas mass in the WHL galaxy clusters. It is estimated to be $\bar{M}_{\text{gas},500} \sim 0.9 \times 10^{13} h^{-1} \text{M}_\odot$. This provides a gas mass fraction of $f_{\text{gas},500} = M_{\text{gas},500}/M_{500} = 0.09 \pm 0.02$ given their average total mass of $M_{500} \sim 1.0 \times 10^{14} h^{-1} \text{M}_\odot$.

7. Discussion and conclusion

In this paper, we present the detection of the kSZ signal with a significance of $\sim 4.9\sigma$. The measurement was performed by stacking the latest *Planck* temperature map at 217 GHz at the positions of the galaxy clusters constructed from the SDSS galaxies. Simple stacks cancel out the kSZ signals because galaxy clusters have an equal probability of having positive or negative kSZ signals. Thus, to avoid this cancellation and align the signs of the kSZ signals, we used the LOS velocities of the WHL galaxy clusters. This approach has an additional advantage: other components such as CMB, CIB, and tSZ have all positive signs and are canceled by the stacking approach. The contamination level of these foreground emissions was studied in T21, showing that it is minor.

To estimate the LOS velocities of the WHL galaxy clusters, we used a machine-learning approach. In this method, we trained our network to learn the correlation between the LOS velocities of galaxy clusters and their surrounding galaxies with a convolutional neural network. To apply our trained model to real data of the WHL galaxy clusters and their surrounding SDSS galaxies, the training was performed on mocks constructed from the Magneticum hydrodynamical simulations.

Our new approach of estimating the LOS velocities has two main advantages. The LOS velocities of the WHL galaxy clusters were estimated in T21 by relying on the galaxy bias value of the SDSS galaxies derived from other studies (Parejko et al. 2013; White et al. 2011; Nuza et al. 2013; Rodríguez-Torres et al. 2016). By contrast, our present model does not need the galaxy bias value, which is implicitly learned by the training process. Moreover, our present model reduces the uncertainty in our LOS velocity estimates due to RSD. These advantages contribute to the increase of the signal-to-noise in our kSZ measurements from ~ 3.5 in T21 to ~ 4.7 . Furthermore, the signal-to-noise is improved to ~ 4.9 by using the latest *Planck* map from the *Planck* 2020 data release.

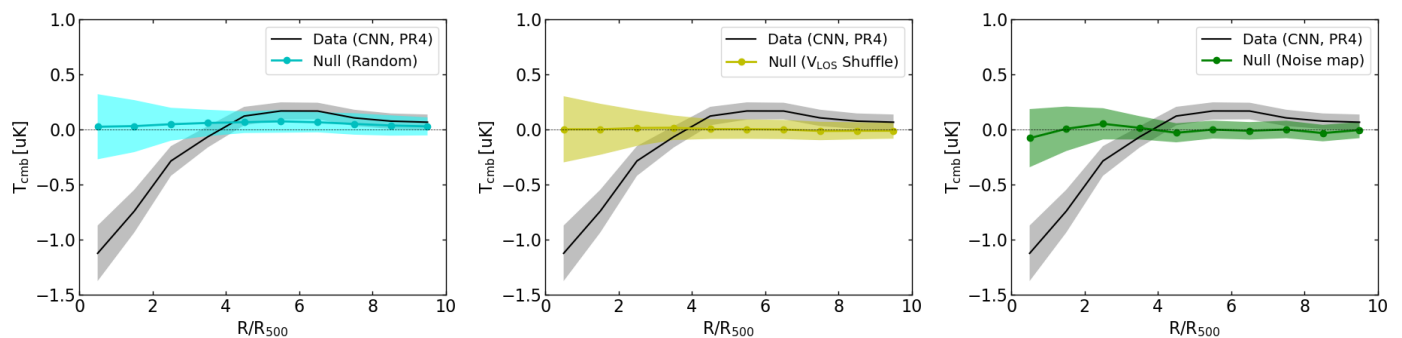


Fig. 5. Velocity-weighted kSZ radial profile around the 30,431 WHL galaxy clusters with the *Planck* PR4 temperature map at 217 GHz (black) compared to three null tests. In the *left* panel, the clusters are displaced at random positions on the *Planck* map, and then stacked. This process is repeated 1,000 times and the mean of the 1,000 random samples is computed (cyan). The 1σ uncertainty is estimated by computing a standard deviation of the 1,000 random samples. The *middle* panel shows the results from cluster stacking after randomly shuffling the LOS velocities of the clusters; this process is repeated 1,000 times and the mean of the 1,000 velocity-shuffled profiles is computed (yellow). The 1σ uncertainty is estimated by computing a standard deviation of the 1,000 velocity-shuffled profiles. In the *right* panel, the clusters are stacked with a noise map produced by $(T_{217}^{\text{HM1}} - T_{217}^{\text{HM2}})/2$, where $T_{217}^{\text{HM1(2)}}$ is the half mission 1(2) *Planck* map at 217 GHz (green). The 1σ uncertainty is estimated by a bootstrap resampling.

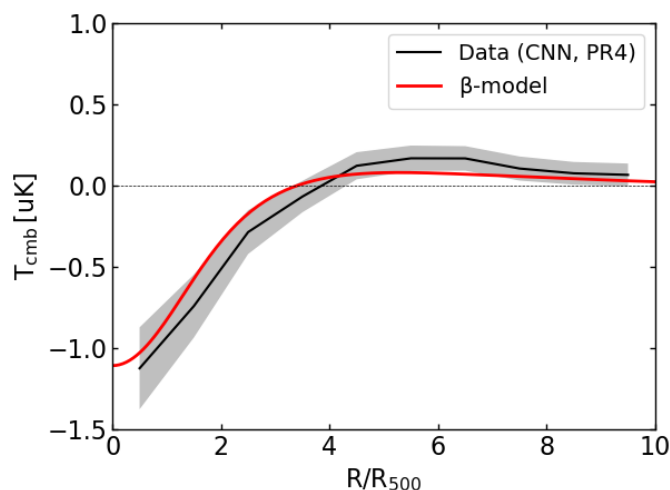


Fig. 6. Velocity-weighted kSZ radial profile around the 30,431 WHL galaxy clusters with the *Planck* PR4 temperature map at 217 GHz (black), fitted with the β model (red).

Based on our new kSZ measurement, we estimated the average optical depth and found $\bar{\tau}_{e,500} = (2.0 \pm 0.4) \times 10^{-3}$ for galaxy clusters with mass of $M_{500} \sim 1.0 \times 10^{14} h^{-1} M_{\odot}$ assuming a β model. This provides an average gas fraction of $f_{\text{gas},500} = 0.09 \pm 0.02$ within R_{500} , which is a bit lower than but consistent with the value in T21 of $f_{\text{gas},500} = 0.12 \pm 0.04$. We also compared our value of the gas fraction with that from the Magneticum hydrodynamic simulations. The Magneticum simulation gives $f_{\text{gas},500} \sim 0.13$ for the same mass of galaxy clusters. We also checked with the IllustrisTNG (TNG300-1) (Nelson et al. 2019), giving $f_{\text{gas},500} \sim 0.13$. Our value is slightly lower than the predictions from these hydrodynamic simulations but, again, consistent within $\sim 2\sigma$.

Moreover, we compared our value with the measurements from X-rays (Gonzalez et al. 2013) ($f_{\text{gas},500} \sim 0.1$ for galaxy clusters with $M_{500} \sim 1.0 \times 10^{14} M_{\odot}$), including *XMM-Newton* and *Chandra* observations from Vikhlinin et al. (2006), Sun et al. (2009), and Sanderson et al. (2013), and kSZ (Soergel et al. 2016) ($f_{\text{gas},500} = 0.08 \pm 0.02$ for galaxy clusters with $M_{500} \sim (1 - 3) \times 10^{14} M_{\odot}$). These results are consistent with

our findings. On the other hand, Lim et al. (2020) claims that the gas fraction in halos is approximately equal to the universal baryon fraction down to low-mass halos with $2 \times 10^{12} M_{\odot}$. The difference may come from the sample selection, for example, due to the difference in cluster redshifts. Lim et al. (2020) studied a cluster sample at $z < 0.12$, while our sample and the sample in Soergel et al. (2016) is at $z \sim 0.5$. Thus, the evolution of the gas in halos may explain the difference in the kSZ measurements. However, the X-ray measurements in Gonzalez et al. (2013) were also applied to local clusters at $z \sim 0.1$, and the evolution does not seem to explain the difference. Recently Schaan et al. (2021) detected the kSZ signals at $\sim 6.5\sigma$ using the Atacama Cosmology Telescope (ACT) DR5 data. Applying our new approach to the ACT data may improve the signal-to-noise of the kSZ measurements and help to understand the discrepancy in the gas mass fraction between (Lim et al. 2020) and (Soergel et al. 2016; Gonzalez et al. 2013). So far, the reason for the discrepancy is unknown, and more precise measurements of gas are necessary in order to make firm conclusions.

Acknowledgements. This research has been supported by the funding for the ByoPiC project from the European Research Council (ERC) under the European Union’s Horizon 2020 research and innovation programme grant agreement ERC-2015-AdG 695561. The authors acknowledge fruitful discussions with the members of the ByoPiC project (<https://byopic.eu/team>). Furthermore, S.Z. acknowledges support by the Israel Science Foundation (grant no. 255/18). This publication used observations obtained with *Planck* (<http://www.esa.int/Planck>), an ESA science mission with instruments and contributions directly funded by ESA Member States, NASA, and Canada. The authors thank Klaus Dolag and Antonio Ragagnin for providing the Magneticum simulations.

References

- Adam, R., Bartalucci, I., Pratt, G. W., et al. 2017, *A&A*, 598, A115
- Alonso, D., Louis, T., Bull, P., & Ferreira, P. G. 2016, *Phys. Rev. D*, 94, 043522
- Anderson, M. E., Gaspari, M., White, S. D. M., Wang, W., & Dai, X. 2015, *MNRAS*, 449, 3806
- Arnaud, M., Pratt, G. W., Piffaretti, R., et al. 2010, *A&A*, 517, A92
- Bhattacharya, S. & Kosowsky, A. 2008, *Phys. Rev. D*, 77, 083004
- Bianchini, F. & Silvestri, A. 2016, *Phys. Rev. D*, 93, 064026
- Cavaliere, A. & Fusco-Femiano, R. 1978, *A&A*, 70, 677
- Chollet, F. 2018, *Deep Learning with Python* (Manning)
- De Bernardis, F., Aiola, S., Vavagiakis, E. M., et al. 2017, *J. Cosmology Astropart. Phys.*, 2017, 008
- Dolag, K. 2015, in *IAU General Assembly*, Vol. 29, 2250156
- Gonzalez, A. H., Sivanandam, S., Zabludoff, A. I., & Zaritsky, D. 2013, *ApJ*, 778, 14

- Górski, K. M., Hivon, E., Banday, A. J., et al. 2005, *ApJ*, 622, 759
- Hand, N., Addison, G. E., Aubourg, E., et al. 2012, *Phys. Rev. Lett.*, 109, 041101
- Hernández-Monteagudo, C., Ma, Y.-Z., Kitaura, F. S., et al. 2015, *Phys. Rev. Lett.*, 115, 191301
- Hill, J. C., Ferraro, S., Battaglia, N., Liu, J., & Spergel, D. N. 2016, *Phys. Rev. Lett.*, 117, 051301
- Hirschmann, M., Dolag, K., Saro, A., et al. 2014, *MNRAS*, 442, 2304
- Hogg, D. W. 1999, arXiv e-prints, astro
- Komatsu, E., Smith, K. M., Dunkley, J., et al. 2011, *ApJS*, 192, 18
- Kuruvilla, J. 2021, arXiv e-prints, arXiv:2109.13938
- Kuruvilla, J. & Aghanim, N. 2021, *A&A*, 653, A130
- Le Brun, A. M. C., McCarthy, I. G., & Melin, J.-B. 2015, *MNRAS*, 451, 3868
- Lim, S. H., Mo, H. J., Wang, H., & Yang, X. 2020, *ApJ*, 889, 48
- Ma, Y.-Z. & Zhao, G.-B. 2014, *Physics Letters B*, 735, 402
- Madhavacheril, M. S., Battaglia, N., Smith, K. M., & Sievers, J. L. 2019, arXiv e-prints, arXiv:1901.02418
- Mueller, E.-M., de Bernardis, F., Bean, R., & Niemack, M. D. 2015, *ApJ*, 808, 47
- Nelson, D., Springel, V., Pillepich, A., et al. 2019, *Computational Astrophysics and Cosmology*, 6, 2
- Nguyen, N.-M., Jasche, J., Lavaux, G., & Schmidt, F. 2020, arXiv e-prints, arXiv:2007.13721
- Nuza, S. E., Sánchez, A. G., Prada, F., et al. 2013, *MNRAS*, 432, 743
- Parejko, J. K., Sunayama, T., Padmanabhan, N., et al. 2013, *MNRAS*, 429, 98
- Plagge, T., Benson, B. A., Ade, P. A. R., et al. 2010, *ApJ*, 716, 1118
- Planck Collaboration. 2013, *A&A*, 557, A52
- Planck Collaboration. 2016a, *A&A*, 594, A13
- Planck Collaboration. 2016b, *A&A*, 594, A22
- Planck Collaboration. 2016c, *A&A*, 586, A140
- Planck Collaboration. 2018, arXiv e-prints, arXiv:1807.06207
- Planck Collaboration. 2020a, *A&A*, 641, A4
- Planck Collaboration. 2020b, *A&A*, 643, A42
- Reid, B., Ho, S., Padmanabhan, N., et al. 2016, *MNRAS*, 455, 1553
- Rodríguez-Torres, S. A., Chuang, C.-H., Prada, F., et al. 2016, *MNRAS*, 460, 1173
- Sanderson, A. J. R., O’Sullivan, E., Ponman, T. J., et al. 2013, *MNRAS*, 429, 3288
- Sayers, J., Mroczkowski, T., Zemcov, M., et al. 2013, *ApJ*, 778, 52
- Schaan, E., Ferraro, S., Amodeo, S., et al. 2021, *Phys. Rev. D*, 103, 063513
- Schaan, E., Ferraro, S., Vargas-Magaña, M., et al. 2016, *Phys. Rev. D*, 93, 082002
- Soergel, B., Flender, S., Story, K. T., et al. 2016, *MNRAS*, 461, 3172
- Sugiyama, N. S., Okumura, T., & Spergel, D. N. 2018, *MNRAS*, 475, 3764
- Sun, M., Voit, G. M., Donahue, M., et al. 2009, *ApJ*, 693, 1142
- Sunyaev, R. A. & Zeldovich, I. B. 1980, *ARA&A*, 18, 537
- Sunyaev, R. A. & Zeldovich, Y. B. 1970, *Ap&SS*, 7, 3
- Sunyaev, R. A. & Zeldovich, Y. B. 1972, *Comments on Astrophysics and Space Physics*, 4, 173
- Tanimura, H., Zaroubi, S., & Aghanim, N. 2021, *A&A*, 645, A112
- Vikhlinin, A., Kravtsov, A., Forman, W., et al. 2006, *ApJ*, 640, 691
- Wen, Z. L. & Han, J. L. 2015, *ApJ*, 807, 178
- Wen, Z. L., Han, J. L., & Liu, F. S. 2012, *ApJS*, 199, 34
- White, M., Blanton, M., Bolton, A., et al. 2011, *ApJ*, 728, 126
- Wu, Z., Zhang, Z., Pan, S., et al. 2021, *ApJ*, 913, 2